

# THE SPATIAL VARIATION OF THE INFRARED-TO-RADIO RATIO IN SPIRAL GALAXIES

K. A. MARSH<sup>1</sup> and G. HELOU<sup>2</sup>  
Jet Propulsion Laboratory  
and Infrared Processing and Analysis Center  
California Institute of Technology

Submitted to *Astrophysical Journal*, September 1994

Received: \_\_\_\_\_

*Subject headings:* infrared: galaxies --- galaxies: photometry --  
radio continuum: galaxies

<sup>1</sup> Jet Propulsion Laboratory, MS 306-451, 4800 Oak Grove Drive, Pasadena,  
CA 91109

<sup>2</sup> California Institute of Technology, IPAC 100-22, Pasadena, CA 91125

## Abstract

We have produced two-dimensional maps of the intensity ratio,  $Q_{60}$ , of  $60\ \mu\text{m}$  infrared to 20 cm radio continuum emission, for a set of 25 nearby galaxies, mostly spirals. The ratio maps were obtained from infrared images made using IRAS data with the Maximum Correlation Method, and radio images made using VLA data. Before taking the ratio, the radio images were processed so as to have the same resolution properties as the infrared images; the final spatial resolution in all cases is approximately  $1''$ , corresponding to 1–2 kpc for most galaxies. This resolution represents a significant improvement over previous studies,

Our new high-resolution maps confirm the slow decrease of  $Q_{60}$  with increasing radial distance from the nucleus, but show additional structure which is probably associated with separate sites of active star formation in the spiral arms. The maps show  $Q_{60}$  to be more closely related to infrared surface brightness than to the radial distance,  $r$ , in the galaxy disk. We note also that the  $Q_{60}$  gradients are absent (or, at least, reduced) for the edge-on galaxies, a property which can be attributed to the dilution of contrast due to the averaging of the additional structure along the line of sight.

The results are all in qualitative agreement with the expectations of the diffusion model, whereby the infrared-radio correlation is driven by the formation of massive stars, and the intensity distribution of radio emission is smeared as a result of the diffusion of energetic electrons accelerated during the supernova phase.

# 1 Introduction

Observations of spiral galaxies at far-infrared and centimeter wavelengths have revealed a strong correlation between the flux densities in these two regimes (Dickey & Salpeter 1984; de Jong et al. 1985; Helou, Soifer, & Rowan-Robinson 1985; Sanders & Mirabel 1985). The correlation appears to hold for all galaxies whose far-infrared luminosities are dominated by on-going star formation, including ellipticals with hidden star-forming disks (Wrobel & Heeschen 1988) and distant starburst galaxies at  $z > 0.1$  and  $L_{\text{FIR}} > 10^{11.0}$  (Karoji et al. 1985). This was unexpected, since different mechanisms are responsible for the infrared and radio emission—the infrared represents thermal emission from heated dust, while the radio is dominated by non-thermal synchrotron emission, even though thermal bremsstrahlung plays an important role at frequencies above about 5 GHz (Price & Duric 1992).

Naturally, the result prompted comparisons between the spatial structure of galaxy disks at infrared and radio wavelengths. A close correspondence has been found between the spatial appearance of spiral galaxies in these two wavelength regimes (Wunderlich & Klein 1988; Wainscoat, de Jong & Wesselius 1987), although the infrared-to-radio intensity ratio appears to be enhanced in the central regions (Beck & Golla 1988; Bica, Helou, & Condon, 1989). More recently, Bica & Helou (1990; BH 90) compared the spatial distributions, at 60  $\mu\text{m}$  and 20 cm wavelength, for 25 galaxies (24 late-type spirals and 1 irregular), and found that the radio images had the appearance of smeared versions of the infrared images.

The above studies have suggested that the underlying link between infrared and radio emission involves the formation of relatively massive ( $\gtrsim 5M_{\odot}$ ) stars, which heat the infrared-emitting dust, and then accelerate the synchrotron-emitting electrons during the subsequent

supernova phase. On the question of why the infrared-radio correlation should be so tight, Helou and Bicay (1993) have suggested that this comes about because the dust-heating photons and relativistic electrons are generated in the same proportions in all galaxies, and there is a close coupling between magnetic field strength and gas density. An alternative explanation has been advanced by Bettens *et al.* (1993), who have invoked a feedback mechanism in which the cosmic-ray electrons (generated by the supernova) influence the subsequent star-formation rate in molecular clouds, via ionization effects. For any of these models, the smearing of the radio images finds a natural explanation in terms of the diffusion of the synchrotron-emitting electrons before they are subsequently lost to radiative decay or escape (131190).

The infrared images on which the 111190 study was based were derived directly from the raw detector data from the Infrared Astronomy Satellite (IRAS), which were of rather coarse spatial resolution ( $1'.5 \times 4'.7$ ). Since the latter dimension was comparable to the sizes of the galaxies themselves, the study was basically 1-dimensional in terms of spatial resolution. In this paper we describe an improved approach to the study of the spatial properties of the infrared-radio correlation using infrared data of higher spatial resolution ( $\sim 1'$  in both coordinates).

## 2 Data

The galaxy sample used in the current investigation consisted of the same 25 galaxies studied by BH90. Our input data for each galaxy consisted of

- (1) Radio continuum image at 20 cm wavelength (frequency 1.49 GHz) made using the

VLA, and described by Condon (1987). The CLEAN algorithm was applied to the maps, with circular Gaussian restoring beams of full-width at half-maximum (FWHM) 0'.8, 0'.9, or 1'.0.

(2) Infrared continuum image at 60  $\mu\text{m}$  wavelength, made using data from the Infrared Astronomy Satellite (IRAS), and the imaging technique known as the Maximum Correlation Method (MCM), described by Aumann, Fowler, and Melnyk (1990). The number of iterations used was 20.

Although the infrared and radio images had comparable spatial resolution ( $\sim 1''$ ), the infrared images were nonisoplanatic. The behavior of their resulting point spread functions (PSFs) was determined by the IRAS scanning geometry, the spatial responses of the set of IRAS detectors that scanned the source, and the inherent properties of the MCM. Since the goal of the study was to compare radio and infrared images at the same spatial resolution, further processing was necessary.

### 3 Analysis Procedure

In order to produce pairs of images (radio and infrared) with the same spatial resolution, we re-CLEANed the radio images and restored them using an effective PSF corresponding to the infrared images. The procedure involved the following steps:

(1) Deconvolve the radio PSF. This step was necessary since the original sets of CLEAN components involved in Condon's (1987) maps were not available. The deconvolution was performed by a reapplication of the CLEAN algorithm, based on the same circular Gaussian beam which Condon had used to restore each map. The image was CLEANed down to

the residual noise level (0.1 mJy/beam), yielding a source model in the form of a set of delta-function components.

(2) Generate synthetic “raw detector data” as would be observed if this source model were scanned using detectors whose spatial responses were the same as for IRAS, and using the same scanning geometry as for the original IRAS observations.

(3) Run these data through the same MCM imaging algorithm as was used to generate the infrared images. The pixel size (1.5"), field of view, and position of the center pixel, were the same as for the corresponding infrared image,

Since the CLEANing operation introduces a small degree of additional smoothing to the radio image as a result of the discretization of component locations, some compensating smoothing was necessary for the infrared image. The form of the smoothing function, whose width was a small fraction of a pixel, was determined numerically. Having applied this compensation, the result in each case was a radio image whose spatial resolution properties were essentially identical to that of the corresponding infrared image.

Because of uncertainties in the absolute positioning of the IRAS data (resulting in errors comparable to a pixel width in the infrared images), it was necessary to perform a final registration step. The required position offset of the infrared image,  $(\Delta\alpha, \Delta\delta)$ , was estimated by minimizing the sum of squares of residuals,  $\phi(\Delta\alpha, \Delta\delta, q)$ , defined by:

$$\phi(\Delta\alpha, \Delta\delta, q) = \sum_{\alpha, \delta} [I_{20\text{cm}}(\alpha, \delta) - q^{-1} I_{60}(\alpha - \Delta\alpha, \delta - \Delta\delta)]^2 \quad (1)$$

where  $I_{20\text{cm}}(\alpha, \delta)$  and  $I_{60}(\alpha, \delta)$  represent the intensity distributions at wavelengths 20 cm and 60  $\mu\text{m}$ , respectively, as a function of right ascension,  $\alpha$ , and declination,  $\delta$ , and  $q$  is a scaling factor representing the weighted-mean ratio of infrared to radio intensity. The summation

was performed over all positions which fell within a rectangular box, constructed so as to include the galaxy but exclude background sources.

The final numerical step was to calculate the infrared-to-radio intensity ratio,  $Q_{60} = I_{60}/I_{20\text{cm}}$ , as a function of position. This quantity was then plotted, in the form of a greyscale image, for all positions for which  $Q_{60} \geq 3\sigma_Q$ , where  $\sigma_Q$  is the standard deviation in  $Q$ . The quantity  $\sigma_Q$  was determined by the noise levels in the infrared and radio images, which were dominated by the dynamic ranges of the processed radio maps, typically 70:1.

## 4 Plots of $Q_{60}$ , and associated discussion

Figure 1 (a- d) shows the results for all 25 galaxies, in the form of plots of  $Q_{60}$ , each of which is shown alongside a plot of infrared surface brightness,  $I_{60}$ . The peak value of  $Q_{60}$  on each plot (denoted  $Q_{\text{peak}}$ ) is listed in Table 1. Examination of the plots shows that in nearly all cases, there is a local maximum in  $Q_{60}$  coincident with the galactic nucleus, as found by BII90. The principal exceptions to this behavior were IC 10 (an irregular galaxy) and NGC 3031 (a disk galaxy with a strong Seyfert nucleus), neither of which were expected to fit the model. In order to illustrate different aspects of the behavior of  $Q_{60}$ , we have plotted the data in the form of histograms, azimuthal y averaged profiles, and scatter plots. For each of these plots, points which fell within one beamwidth (1') of a confusing point source on the radio maps (as identified by Condon 1987) were excluded.

## 4.1 Histograms

Histograms of  $Q_{60}$  values for each galaxy are presented in Figure 2. The frequency of occurrence of  $Q_{60}$  in the histograms has been weighted by radio intensity, so that the resulting mean value of  $Q_{60}$  (denoted  $\bar{Q}_{60}$ ) corresponds to the global flux ratio of 60  $\mu\text{m}$  to 20 cm emission.

The histograms show that this sample of galaxies exhibits a spread of values of both the mean,  $\bar{Q}_{60}$ , and width of the distribution for each galaxy. The range of  $\bar{Q}_{60}$  values (100–300) is consistent with the values found by BII90. The widths of the distributions show a considerably greater range, from the narrow distributions such as NGC 891 and NGC 1569 (both of which have FWHM's of approximately 20) to the much broader distributions of galaxies such as NGC 3621 and NGC 4303, with FWHM's of approximately 200 and 300, respectively. A comparison between the histogram plots and Figure 1 shows that there is a distinct tendency for edge-on galaxies (e.g. NGC 891, NGC 4565, and NGC 5907) to have narrow histograms, i.e. small variations of  $Q_{60}$  across the galaxy. This is consistent with the spread being due in large measure to the contrast between various parts of the disk; when the disk is viewed edge-on, the contrast is diminished or diluted because the line of sight averages over various disk regions,

## 4.2 Azimuthally averaged profiles

Azimuthally-averaged profiles of  $Q_{60}$  as a function of radial distance,  $r$ , from the nucleus are presented in Figure 3. The values of  $Q_{60}$  were averaged in elliptical annuli on the sky (circular in the plane of the galaxy). The nucleus was taken as the position of peak infrared



intensity.

The averaged radial profiles of  $Q_{60}$  confirm the result found by BH90, whereby  $Q_{60}$  decreases more-or-less monotonically outward from the nucleus. One exception, already noted by BH90, is NGC 3031, whose Seyfert nucleus produces enhanced radio emission which results in a strong central depression in  $Q_{60}$ . Other exceptions are the edge-on galaxies, such as NGC 891, NGC 4565, and NGC 5907, whose  $Q_{60}$  profiles are essentially flat. The lack of  $Q_{60}$  gradients for these galaxies is also quite apparent from the 2-dimensional images of Figure 1. If we assume that their intensity distributions are described by the diffusion model, with a diffusion scale comparable to other galaxies in the sample, then the above behavior is inconsistent with simple radial exponential models for the radio and infrared intensity distributions, since such distributions produce very little softening of the observed gradients with increasing inclination of the galaxy. With more complicated intensity distributions, however, one might explain the effect in terms of the contrast-dilution mentioned above, whereby radial trends in  $Q_{60}$  are diluted by the superposition of other emission regions along the line of sight. We will examine this hypothesis quantitatively in Section 5, using estimates of the gradients.

### 4.3 Scatter plots

Scatter plots of  $Q_{60}$  were constructed as a function of  $r$ , and as a function of infrared surface brightness,  $I_{60}$ . For these plots, the spatial sampling interval was chosen to correspond to the resolution of the images (1' in both orthogonal axes), in order to ensure that each point represents essentially independent information. The scatter plots are presented in pairs, and

are shown in Figure 4 (a--e).

The interpretation of the scatter plots is aided by a comparison with the 2-dimensional  $Q_{60}$  plots of Figure 1. The latter plots show that, besides the large-scale radial decrease in  $Q_{60}$ , there is, in many cases, an additional effect superposed on the general trend, in the form of off-nucleus local maxima which coincide with local maxima, in  $I_{60}$ . These new details are seen in the well-resolved face-on spirals, and are particularly prominent, in NGC 5194, NGC 5236, and NGC 6946. They also appear in some edge-on spirals, such as NGC 4631. These local maxima correspond to locally prominent star formation regions in the spiral arms. The new features cannot be accounted for in the simple model by Helou and Bicay (1993), which describes the  $I_{60}$  distribution as an exponential disk. They therefore partially destroy the predicted gradient of  $Q_{60}$  as a function of  $r$ . This is clearly visible in the scatter plots. The essential content, however, of the Helou & Bicay model is not in the exponential disks, but in the physics of diffusion, escape and decay of cosmic-ray electrons, and the effects on the appearance of the radio map. These effects should apply locally to each center of star formation activity, and cause the ratio  $Q_{60}$  to fall with increasing distance from each center. Since  $I_{60}$  also falls with increasing distance from a center of activity, one would expect  $Q_{60}$  and  $I_{60}$  to be positively correlated. We can test this hypothesis by comparing the scatter plots of  $Q_{60}$  v.  $r$  with those of  $Q_{60}$  v.  $I_{60}$ . The plots are consistent with our expectations, i.e.  $Q_{60}$  is more closely related to infrared surface brightness than to the radial distance in the galaxy disk.

## 5 Estimates of Gradients

In order to make quantitative comparisons of the radial gradients of  $Q_{60}$ , the large-scale variations of  $I_{60}$  and  $Q_{60}$  in the galactic disks were represented in terms of radial exponentials with e-folding distances  $\ell_{\text{disk}}$  and  $\ell_Q$ , respectively. If we denote the intrinsic (as opposed to observed) values of  $I_{60}$  and  $Q_{60}$  by  $\tilde{I}_{60}$  and  $\tilde{Q}_{60}$ , respectively, then, on the basis of the assumed functional forms, the ratio  $\ell_{\text{disk}}/\ell_Q$  represents the relative radial gradient of  $\ln \tilde{Q}_{60}$  with respect to the gradient of  $\ln \tilde{I}_{60}$ , i.e.

$$\frac{\ell_{\text{disk}}}{\ell_Q} = \frac{d \ln \tilde{Q}_{60}(r)}{dr} \bigg/ \frac{d \ln \tilde{I}_{60}(r)}{dr} \quad (2)$$

In the limit of high spatial resolution,  $\ell_{\text{disk}}/\ell_Q$  would also correspond to the slope of a  $\log Q_{60}$  v.  $\log I_{60}$  scatter plot in Figure 4, assuming that the galaxy brightnesses are well-represented by radial exponentials.

The observed data were used to obtain maximum-likelihood estimates of  $\ell_{\text{disk}}$  and  $\ell_Q$ . The  $\ell_{\text{disk}}$  estimates took account of the point spread function, using a measurement model of the form:

$$I_{60}(\mathbf{r}) = [I_0 \exp(-r/r_0)] * h(\mathbf{r}) + \xi(\mathbf{r}) \quad (3)$$

where

$$r_0 = \ell_{\text{disk}} \cos i / [1 - (x \sin \theta + y \cos \theta)^2 \sin^2 i / r^2]^{\frac{1}{2}} \quad (4)$$

such that  $\mathbf{r}$  is a 2-dimensional angular position vector of magnitude  $r = \sqrt{x^2 + y^2}$  where  $x$  and  $y$  represent the right ascension and declination offsets from the galactic nucleus,  $i$  and  $\theta$  are the inclination and position angle of the tilt axis of the galactic disk, respectively,  $h(\mathbf{r})$  is the point spread function, and ‘\*’ represents convolution. The quantity  $\xi(\mathbf{r})$  is a random

variable representing a combination of model error and measurement noise. It is assumed to be a Zero-mean Gaussian process whose standard deviation is proportional to  $I_{60}$ . The latter condition ensures that shape information contained in the low-intensity portion of the disk receives as much weight as that of high-intensity features such as the nucleus and inner disk.

Estimation of  $\ell_Q$ , with similar allowance for the point spread function, would be complicated by the fact that the measured  $Q_{60}$  values are not related to the true values by simple convolution. Therefore, a simpler procedure was adopted, in which the estimates of  $\ell_Q$  were made using simple least squares fits of  $Q_{60}$  as a function of  $r$ , using the data from the radial plots of Figure 3.

The results of the fits are presented in Table 1, in the form of the estimated values of  $\ell_{\text{disk}}$  and  $\ell_{\text{disk}}/\ell_Q$ . Next to the  $\ell_{\text{disk}}/\ell_Q$  values are the corresponding values from B1190, for comparison. Also included in the Table are the values of the inclination,  $i$ , of the disk with respect to the plane of the sky, taken from B1190. The irregular galaxy IC 10 was not included in this part of the analysis since it does not provide a meaningful fit to an exponential disk. In the case of NGC 3031, the central portion was omitted from the fit because of the effects of the enhanced radio emission from the Seyfert nucleus. It is apparent from the values of  $\ell_{\text{disk}}/\ell_Q$  that  $Q_{60}$  falls off much more slowly than the brightness of the disk, in agreement with B1190. However, it is also apparent that in more than half of the cases, the present values of  $\ell_{\text{disk}}/\ell_Q$  are significantly larger than those obtained by B1190. The discrepancy lies in the values of  $\ell_Q$  rather than  $\ell_{\text{disk}}$ , and we attribute it to spatial dilution effects in the B1190 data, for reasons which will be discussed later.

Figure 5 shows a plot of the relative radial gradient,  $\ell_{\text{disk}}/\ell_Q$ , versus the inclination of the galaxy, using the data from Table 1. The plot shows a distinct, albeit weak, correlation between these two quantities, in the sense that the relative radial gradient decreases with increasing inclination.

The trend is consistent with the explanation, advanced earlier, for the lack of an observable  $Q_{60}$  gradient for the edge-on galaxies. Specifically, the greater the inclination of the galaxy, the greater the number of emission regions which become averaged, within the instrumental beam, along the line of sight, and hence the greater will be the dilution of the  $Q_{60}$  gradients. We have tested the plausibility of this hypothesis by simulating the appearance of edge-on galaxies using 1-dimensional “fan-beam” averages of nearly-face-on galaxies, and examining the corresponding spatial behavior of  $Q_{60}$ . This was carried out for the 9 galaxies with  $i \leq 45^\circ$ ; fan-beam averages “were constructed in two orthogonal directions for each galaxy, making a total of 18 cases. Before the fan-beam averaging, the mean value of relative radial gradient ( $\ell_{\text{disk}}/\ell_Q$ ) was  $0.27 \pm 0.08$ . After the fan-beam averaging, the mean value was reduced significantly, to  $0.13 \pm 0.16$ ; individual values have been plotted on Figure 5. We therefore conclude that the above trend with inclination can be explained by the contrast dilution effect.

The contrast dilution effect also provides an explanation for the fact that the presently-estimated  $Q_{60}$  gradients tend to be larger than those of BH90. The reason is that the spatial resolution in the latter study was much poorer along one axis, resulting effectively in fan-beam averaging along that axis, and, consequently, contrast dilution in the same way as was simulated above. Since contrast dilution makes the estimated gradients resolution-

dependent, caution must be exercised in interpreting the results. Based on higher resolution data from other wavelengths, we would expect the presence of a considerable amount of structure below the resolution limit of the present study, and hence the present data undoubtedly suffer from contrast dilution effects also. For a fixed angular resolution ( $1'$  in the present case), the linear size of the resolution element (in kpc) will be proportional to distance, and since the distances span an order of magnitude (2.9–25.7 Mpc), the degree of contrast dilution will vary greatly over this sample of spiral galaxies. The estimated  $Q_{60}$  gradients are therefore best regarded as lower limits.

## 6 Are the Observed $Q_{60}$ Gradients Real?

Could the radial gradients in  $Q_{60}$  be spurious effects induced by the data reduction? In considering this question, it is important to note that the rectification procedure described in Section 3 was carefully designed to ensure that both the radio and infrared maps possessed the same spatial resolution, so that any observed differences could be attributed to real differences in source structure. It assumed, of course, that the instrumental resolution was known accurately for both radio and infrared. We believe that this is a good assumption, since (a) the spatial resolution of the radio images is determined by the physical spacing of the interferometer dishes and by the width of the restoring beam, both of which are known accurately, and (b) the IRAS detector responses have been carefully measured using observations of point sources (*IRAS Explanatory Supplement 19/38*). The only known source of systematic error in the latter is a truncation of the response at  $\sim 1\%$  of maximum. This error would cause infrared sources to appear slightly broader than they actually are, which

would have the effect of *reducing* any radial gradients in  $Q_{60}$ . Thus this error would not be capable of producing spurious gradients.

Perhaps the best piece of independent evidence for the reality of the radial gradients is that some galaxies do not show the effect at all. If the gradients were simply a result of the radio images possessing more instrumental smearing than the infrared images, then all of the compact infrared sources on the images (e.g., the galactic nuclei) would correspond to similar local radial decreases in  $Q_{60}$ . The fact that some galaxies (e.g., NGC 891, NGC 4565, and NGC 5907) show no  $Q_{60}$  gradients while others (e.g., NGC 4303 and NGC 6946) show a prominent falloff from the nucleus, strongly supports a non-instrumental origin for the gradients.

A piece of statistical evidence for the reality of the gradients is that the  $Q_{60}$  gradients appear to be systematically suppressed for the high-inclination galaxies. Since the calculation of the Z-dimensional  $Q_{60}$  images involved no assumptions about inclination, this argues for an astrophysical origin for the gradients.

## 7 Conclusions

The two principal conclusions from the study are:

1. The previously-reported gradients in  $Q_{60}$  are real, and indeed much softer than the gradients in brightness,  $I_{60}$ . The radial decrease in  $Q_{60}$  is in qualitative agreement with the diffusion model.

2. The radial behavior of  $Q_{60}$  is complicated by the presence of off-nucleus local maxima (probably separate sites of star formation in the spiral arms), each of which behaves as a local center from which  $Q_{60}$  decreases radially. The behavior of  $Q_{60}$  in the vicinity of each local center is in qualitative agreement with the diffusion model.

Because of the off-nucleus local maxima, the global radial behavior of  $Q_{60}$  is of limited usefulness as a quantitative tool for the study of the physical association between infrared and radio emission in the context of the diffusion model. This is especially true of the highly-inclined galaxies because of the line-of-sight averaging effect. The quantitative predictions of the diffusion model could best be studied by comparing the radio images with convolved versions of the infrared images, using various smearing kernels. Such a study will be the subject of a forthcoming paper.

As the spatial resolution of the images is increased in future observations, we expect that a point will be reached at which structural details of the confining magnetic field are resolved, and the convolutional relation will begin to break down. In the case of NGC 253, the mid-IR and radio become decorrelated on spatial scales below about 100 pc (Keto *et al.* 1993). If this scale is representative of the far-IR also, then the spatial resolution of the present images is an order of magnitude too coarse to show such effects. We therefore expect the convolutional relation to be maintained, and will attempt to verify this in our upcoming paper.



## 8 Acknowledgements

We thank M. D. Bica y and Zhong Wang for stimulating discussions, and Diane Engler for running the MCM software. This research has been supported through the IRAS Extended Mission Program by the Jet Propulsion Laboratory, California Institute of Technology, under contract with the National Aeronautics and Space Administration.

Table 1:  $Q_{60}$  data and related parameters

Galaxy	i	$Q_{\text{peak}}$	$\ell_{\text{disk}}$	$\ell_{\text{disk}}/\ell_Q$	$(\ell_{\text{disk}}/\ell_Q)_{\text{BH90}}$
IC 10	33	542	. . .	...	...
NGC 55	78	333	2.667	0.175	0.267
NGC 253	73	497	1.715	0.188	0.183
NGC 628	21	484	1.087	0.317	...
NGC 891	78	136	0.933	0.016	...
NGC 1097	45	152	0.919	0.142	0.105
NGC 1569	59	145	0.393	0.053	..
NGC 2403	52	478	2.497	0.166	...
NGC 2903	58	173	0.656	0.101	0.043
NGC 3031	57	860	2.530	0.305	...
NGC 3344	20	176	0.679	0.194	0.062
NGC 3556	72	181	0.797	0.140	0.143
NGC 3621	49	262	0.779	0.327	0.068
NGC 4254	27	136	0.465	0.209	0.045
NGC 4303	24	311	0.511	0.436	0.045
NGC 4490	5s	76	0.646	0.078	0.068
NGC 4565	80	183	1.522	0.037	...
NGC 4631	77	119	1.490	0.272	0.228
NGC 5055	52	209	0.875	0.247	0.075
NGC 5194	45	137	0.776	0.250	0.086
NGC 5236	24	242	1.031	0.306	0.141
NGC 5907	82	215	1.009	-0.021	...
NGC 6946	27	177	1.039	0.215	0.179
NGC 733 I	68	172	1.522	0.069	
NGC 7793	44	340	0.919	0.329	0.072

## References

- Aumann, H. H., Fowler, J. W. and Melnyk, M. 1990, *AJ*, 100, 1674
- Beck, R. & Golla, G. 1988, *A&A*, 191, L9
- Bettens, R. 1'. A., Brown, R. D., Cragg, D. M., Dickenson, C. J. & Godfrey, P. D. 1993, *MNRAS*, 263, 93
- Bicay, M. D., Helou, G. & Condon, J. J. 1989, *ApJ*, 338, L53
- Bicay, M. D. & Helou, G. 1990, *ApJ*, 362, 59
- Condon, J. J. 1987, *ApJ Suppl.* 65, 485
- de Jong, T., Klein, U., Wielebinski, R., & Wunderlich, F. 1985, *A&A*, 147, L6
- Dickey, J. M. & Salpeter, E. E. 1984, *ApJ*, 284, 461
- Helou, G. and Bicay, M. D. B. 1993, *ApJ*, 415, 93
- Helou, G., Soifer, B. T. and Rowan-Robinson, M. 1985, *ApJ*, 298, L7
- IRAS Catalogs and Atlases, Explanatory Supplement*. 1988, ed. C. A. Beichman, G. Neugebauer, H. J. Habing, P. E. Clegg, and T. J. Chester (Washington, DC: Government Printing Office).
- Karoji, H., Dennefeld, M. & Ukita, N. 1985, *A&A*, 155, 1,3
- Keto, E., Ball, R., Arens, J., Jernigan, G., Meixner, H., Skinner, C., & Graham, J. 1993, *ApJ*, 413, 1,23
- Price, R. & Duric, N. 1992 *ApJ*, 401, 81
- Sanders, D. B. & Mirabel, I. E. 1985, *ApJ*, 298, 1,31
- Wainscoat, R. J., de Jong, T., and Wesselius, P. R., 1987, *A&A*, 181, 225
- Wrobel, J. M. & Heeschen, S. 1988, *ApJ*, 335, 677

Wunderlich, E. & Klein, U. 1988, *A&A*, 206, 47.

### Figure Captions:

Figure 1: The spatial distribution of the 60  $\mu$ m-to-20 cm intensity ratio,  $Q_{60}$ . The left hand plot of each pair represents the 60  $\mu$ m infrared intensity on a logarithmic scale of 2 decades (3 decades for NGC 253); the corresponding right hand plot shows  $Q_{60}$  on a linear scale. The field of view is: (a)-(c) 10' x 10'; (d) 20' x 20'.

Figure 2: Histograms of  $Q_{60}$ , weighted by radio intensity.

Figure 3: Radial profiles of  $\log Q_{60}$ , averaged in elliptical annuli (the projections of circular annuli in the disk-plane) of width 2 pixels (0.5').

**Figure 4:** Scatter plots of  $Q_{60}$  as a function of radial distance from the nucleus,  $r$ , and infrared surface brightness,  $I_{60}$ .

Figure 5: The relative radial gradient of  $Q_{60}$  (represented by  $\ell_{\text{disk}}/\ell_Q$ ) as a function of the inclination of the disk of the galaxy. The filled circles represent values estimated from the 2-dimensional images. The open circles represent simulated values for edge-on galaxies (whereby structure becomes averaged along the line of sight), and were obtained from fan-beam averages of the low-inclination galaxies ( $i \leq 45^\circ$ ). Each open circle represents the mean of the two values obtained from orthogonal averaging directions, and is labeled to enable comparison with the original value, i.e., *before* fan-beam averaging (the corresponding filled circle).

Fig 1 a

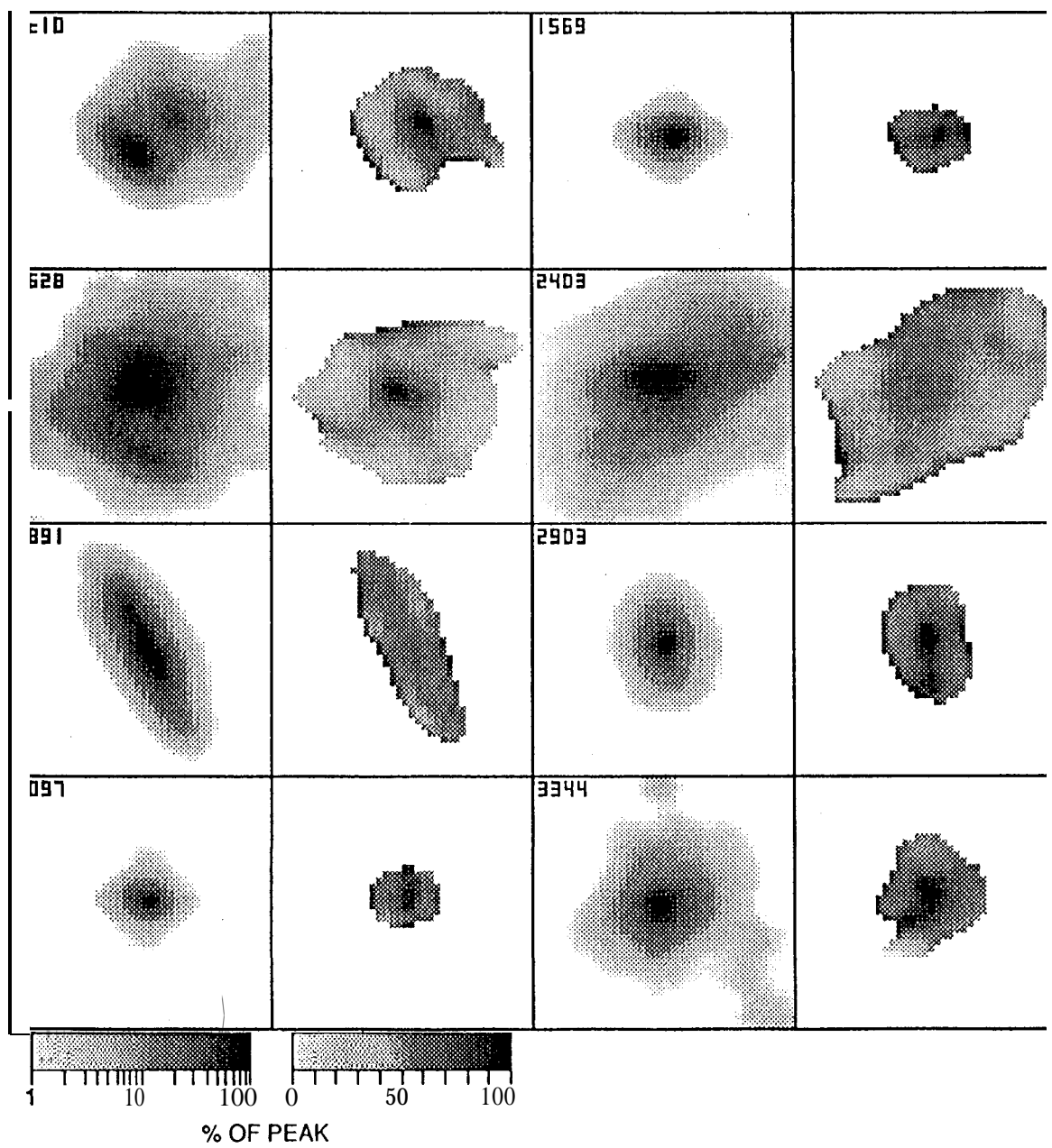


Fig 6

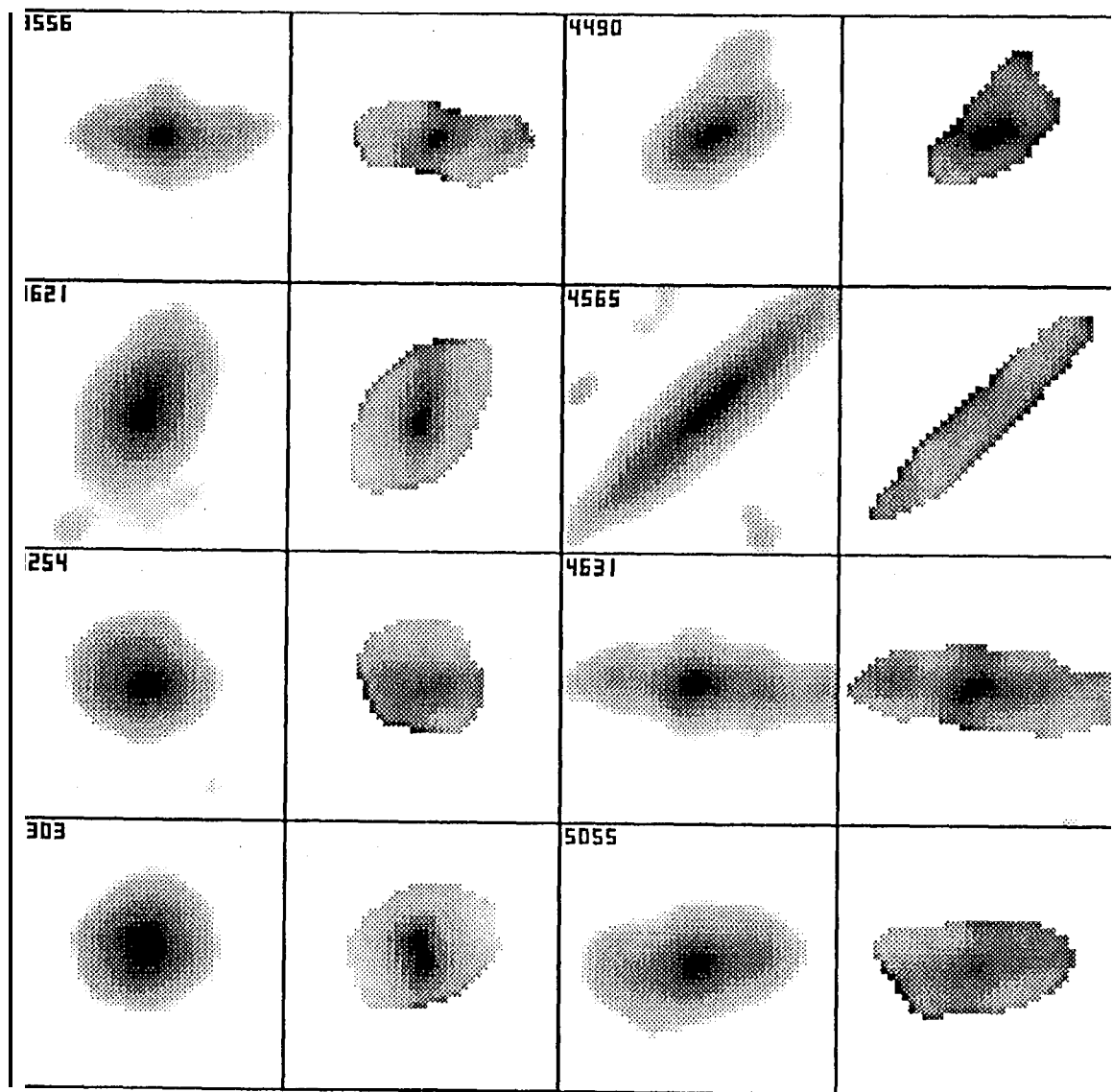


Fig 1 c.

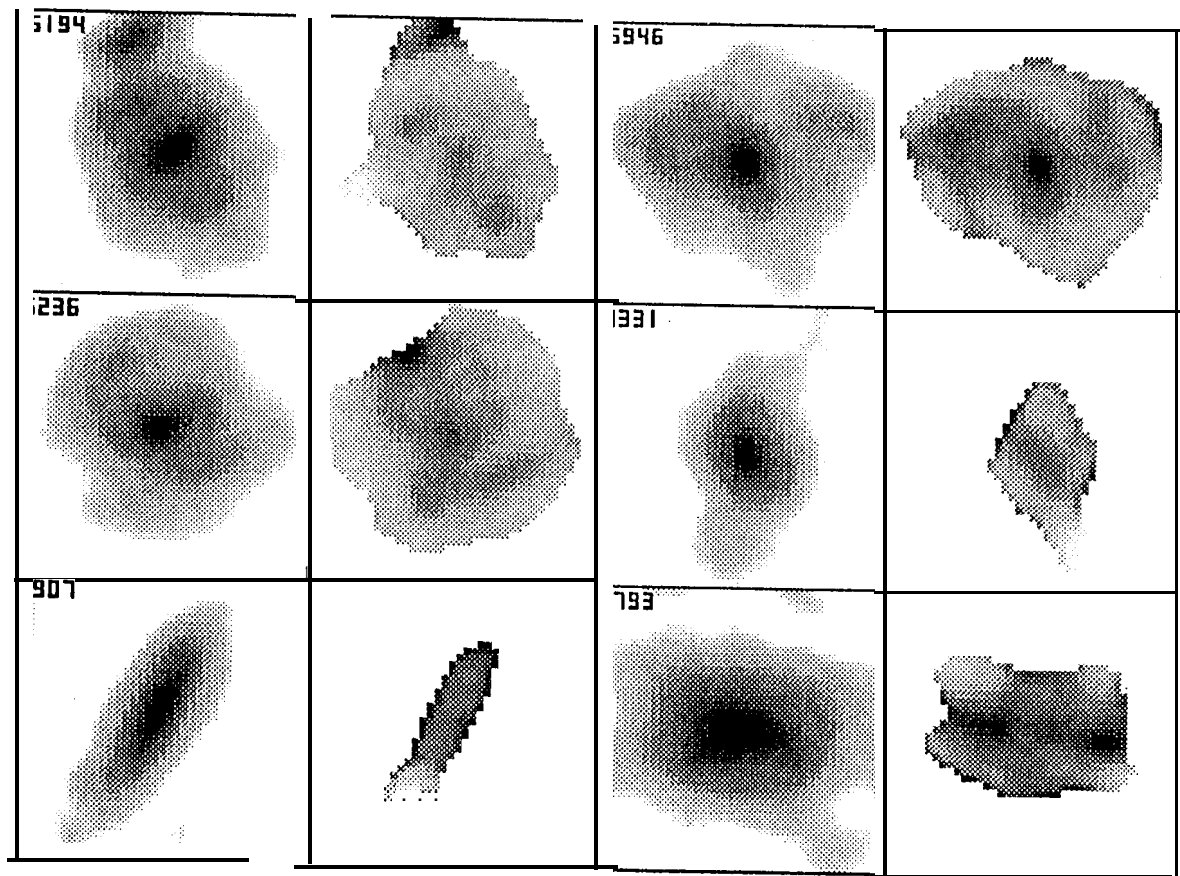




Fig 1 d

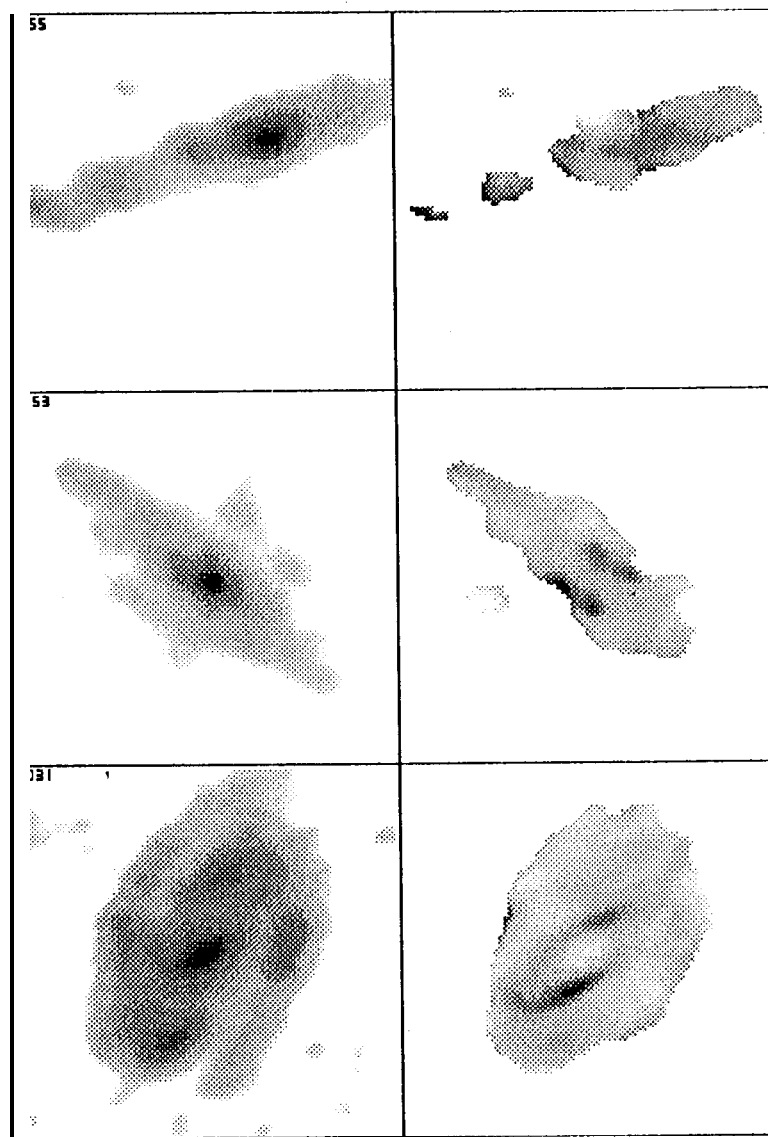


Fig 2

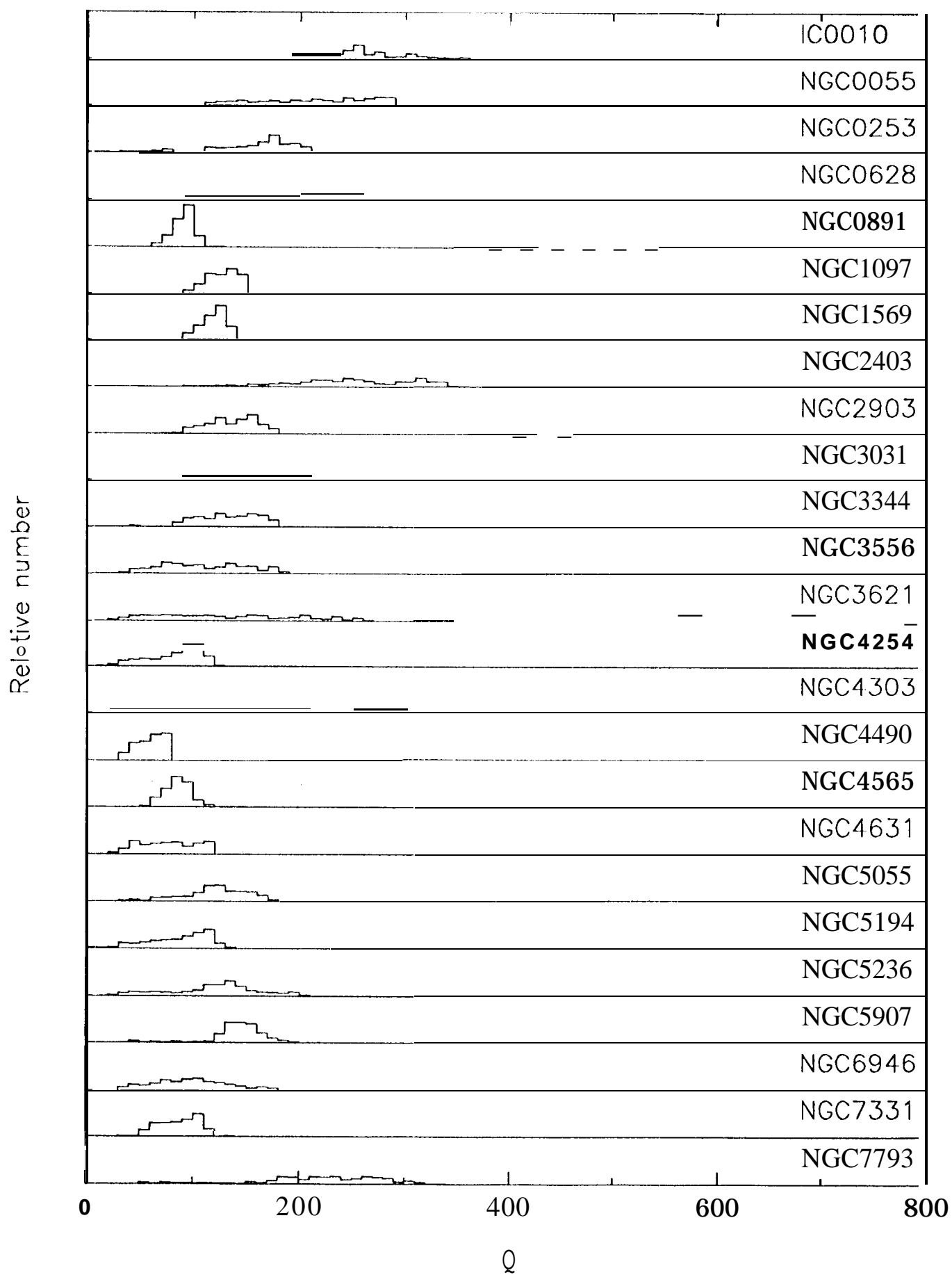


Fig 3 a

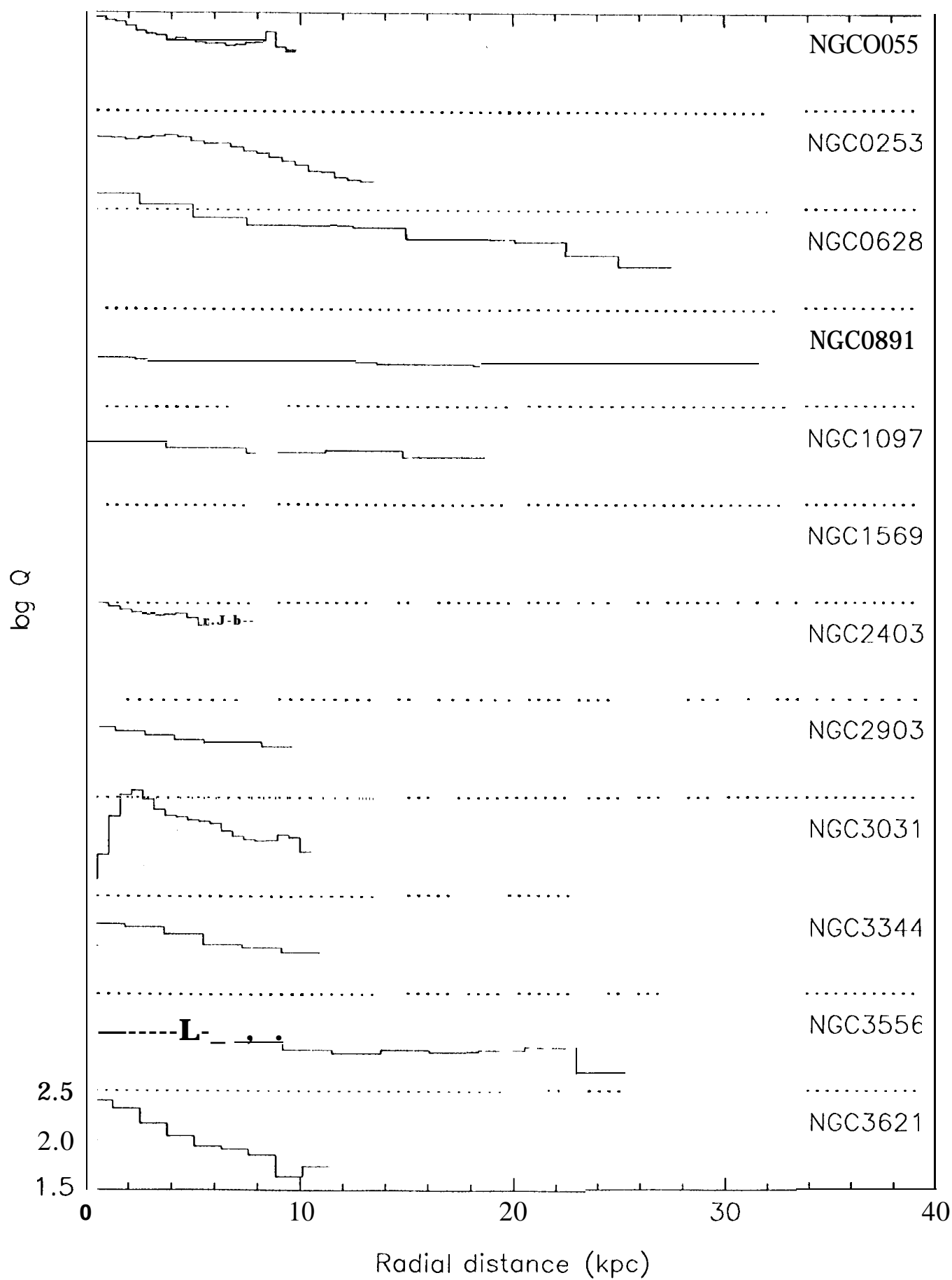


Fig 3b

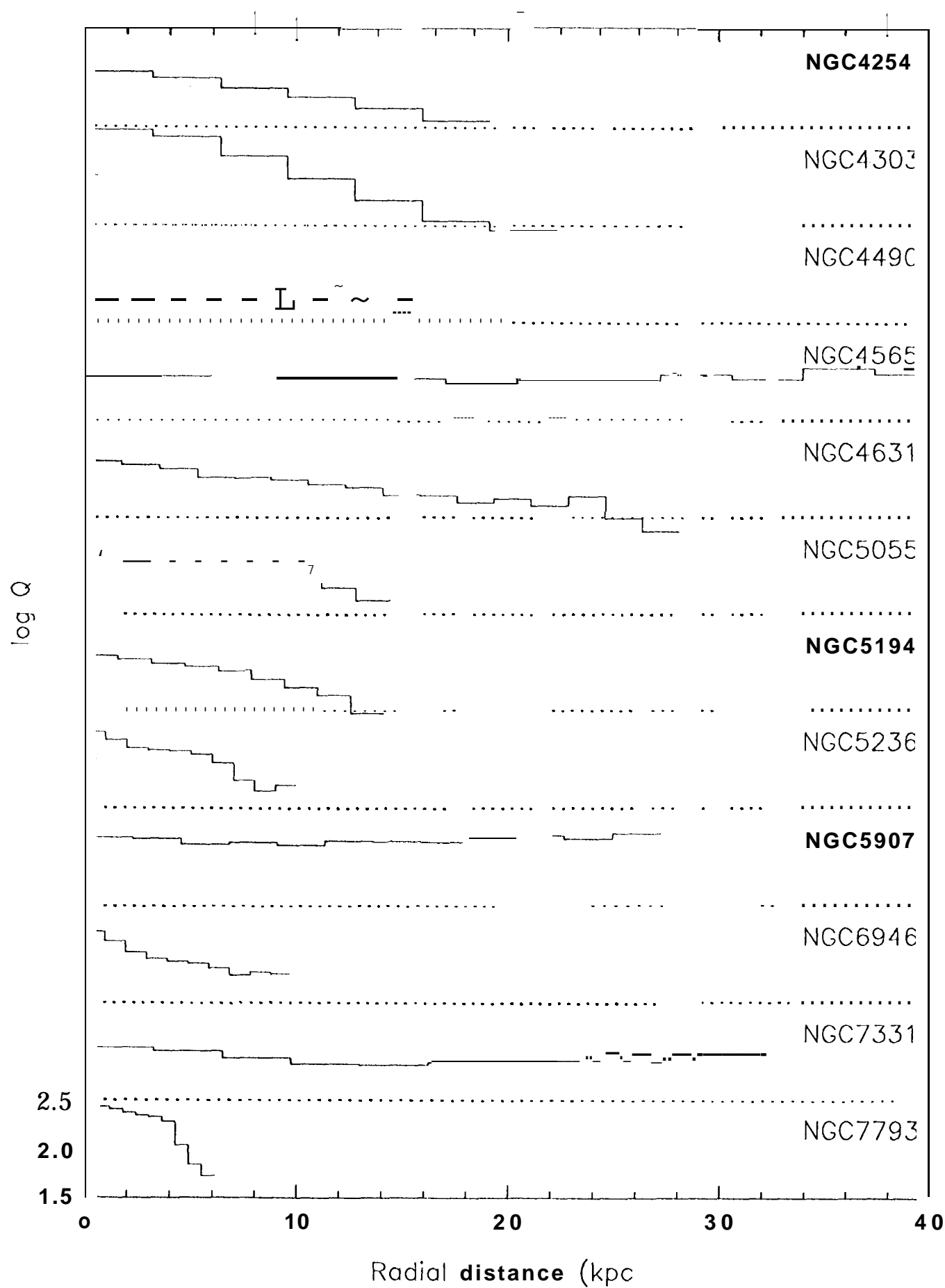


Fig 4a

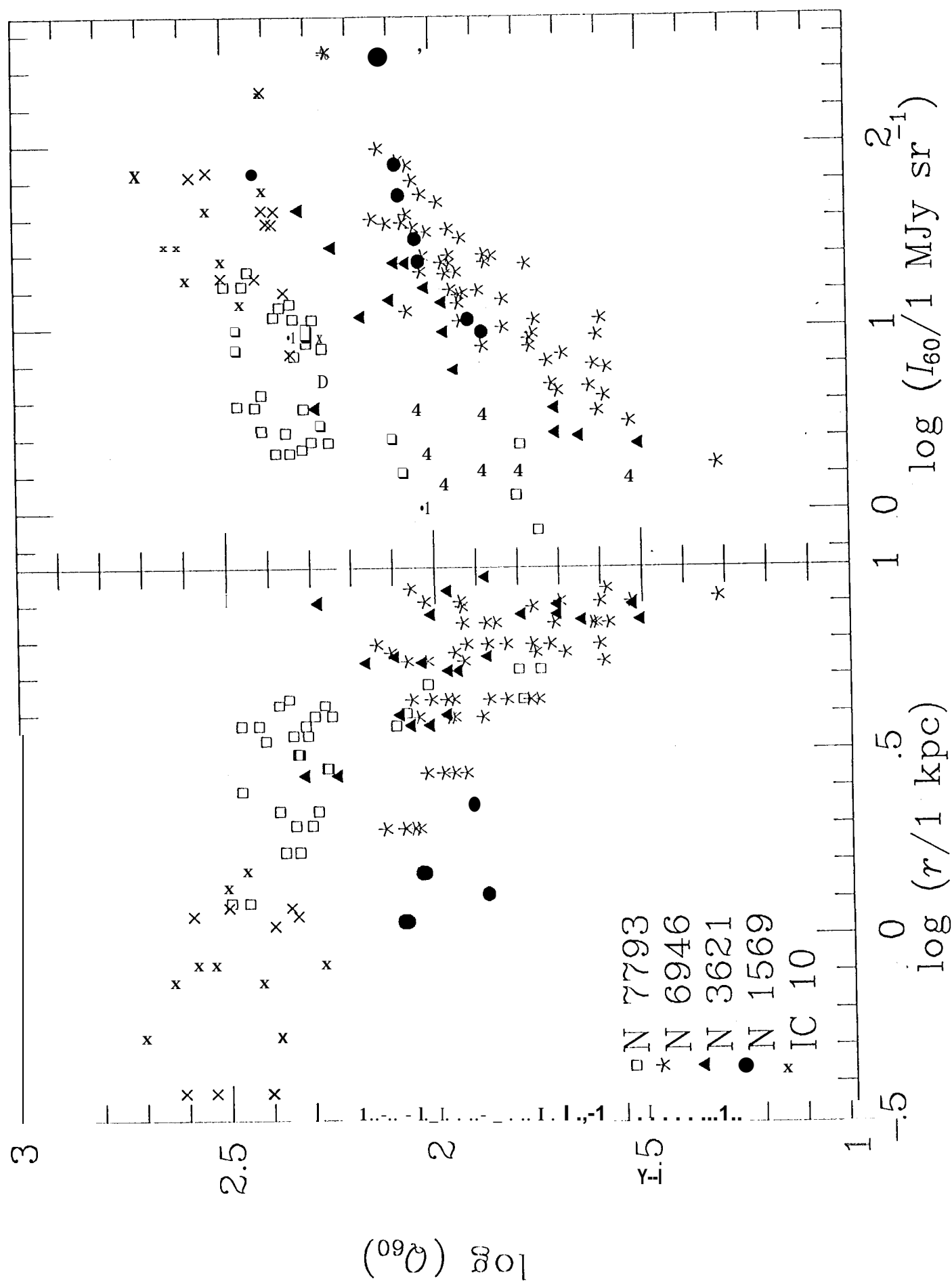
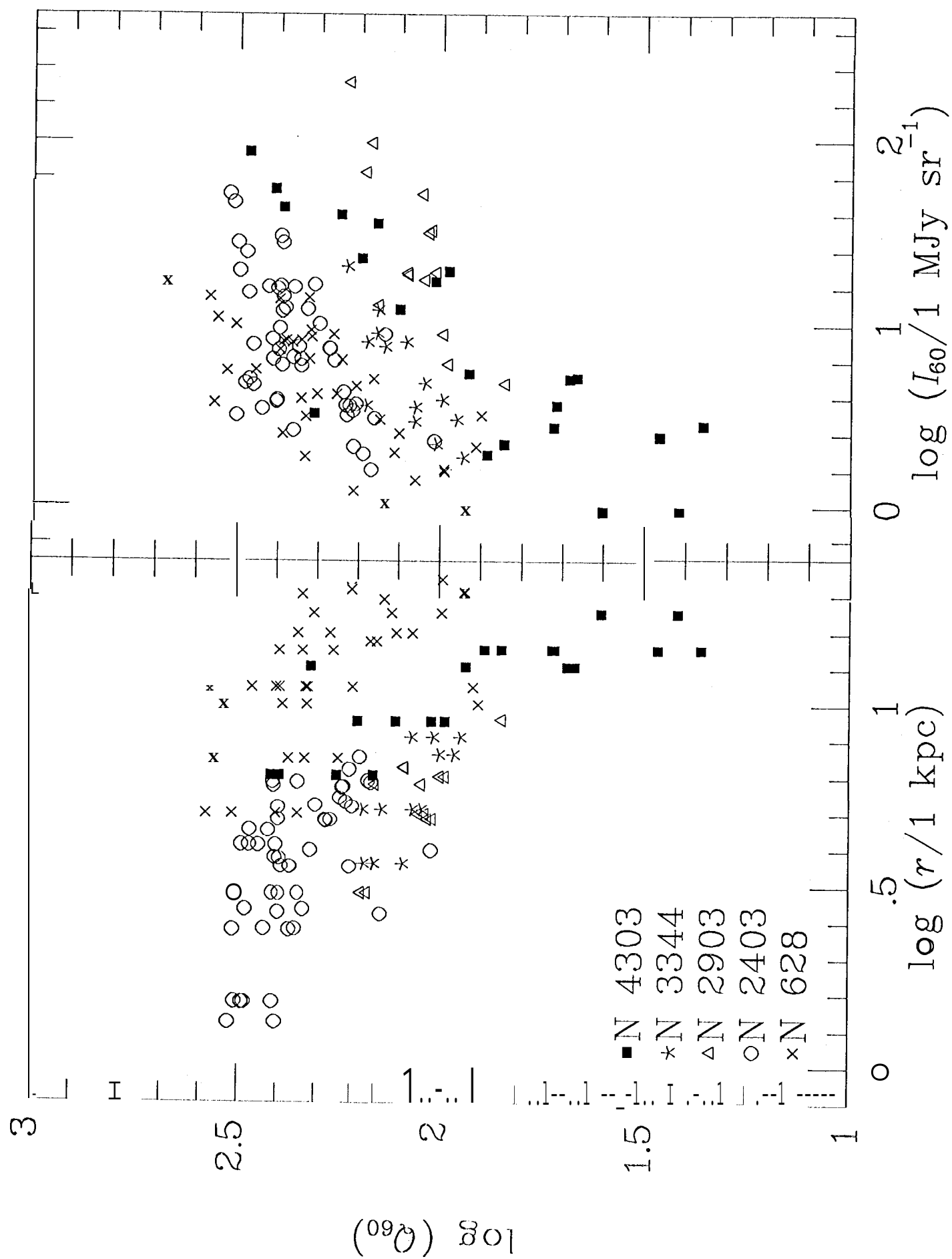
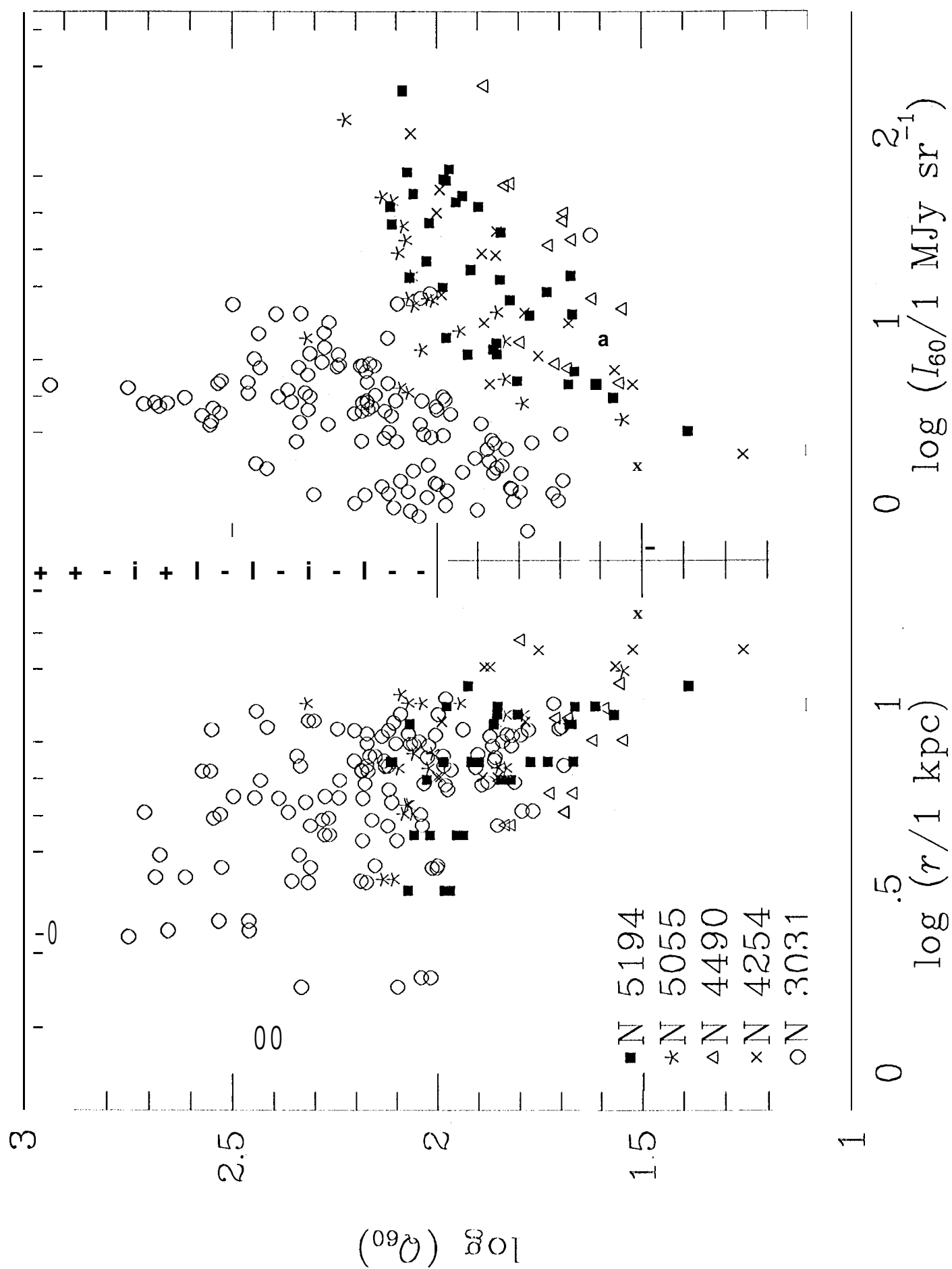


Fig 4b





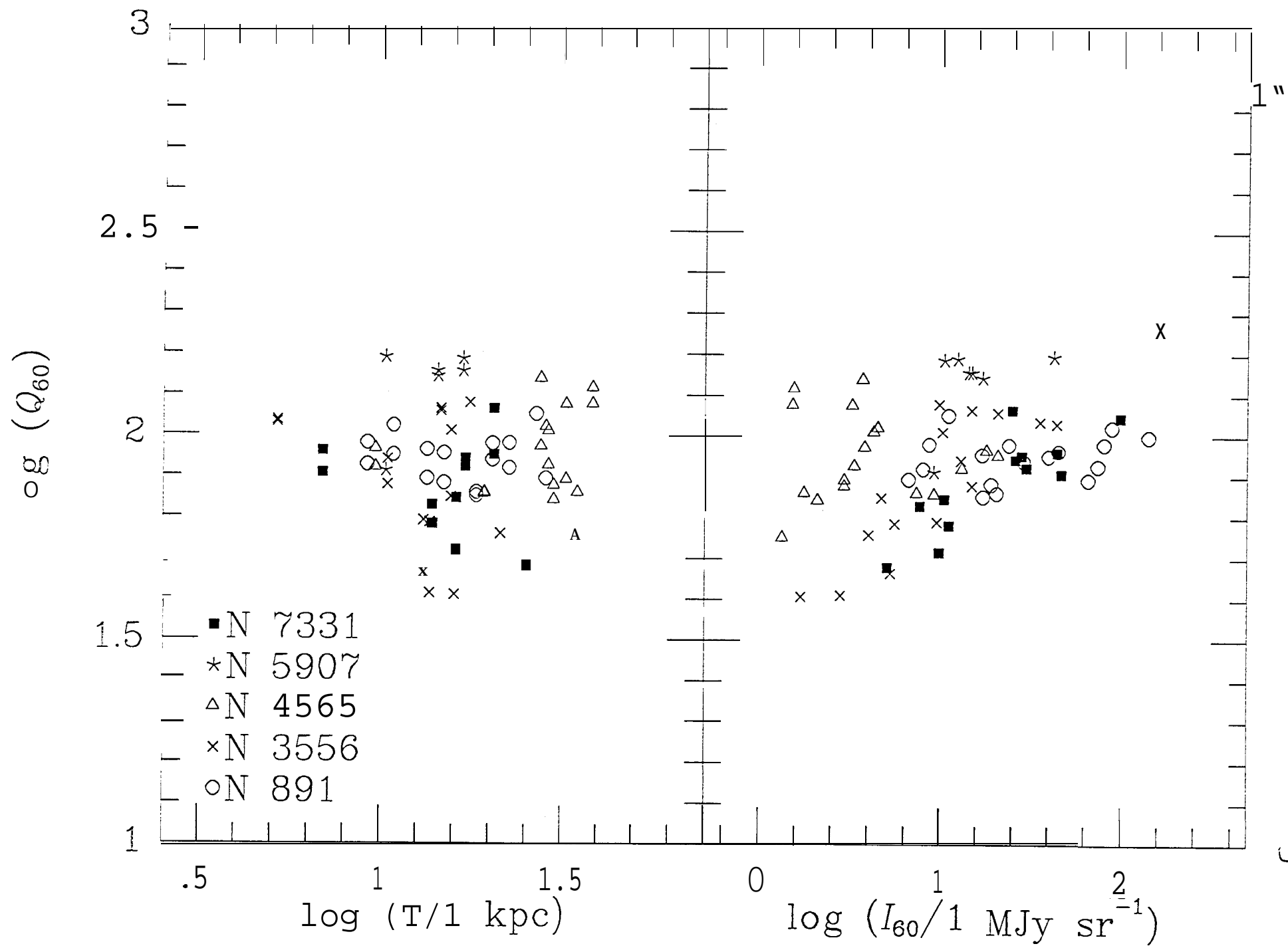


Fig 4d



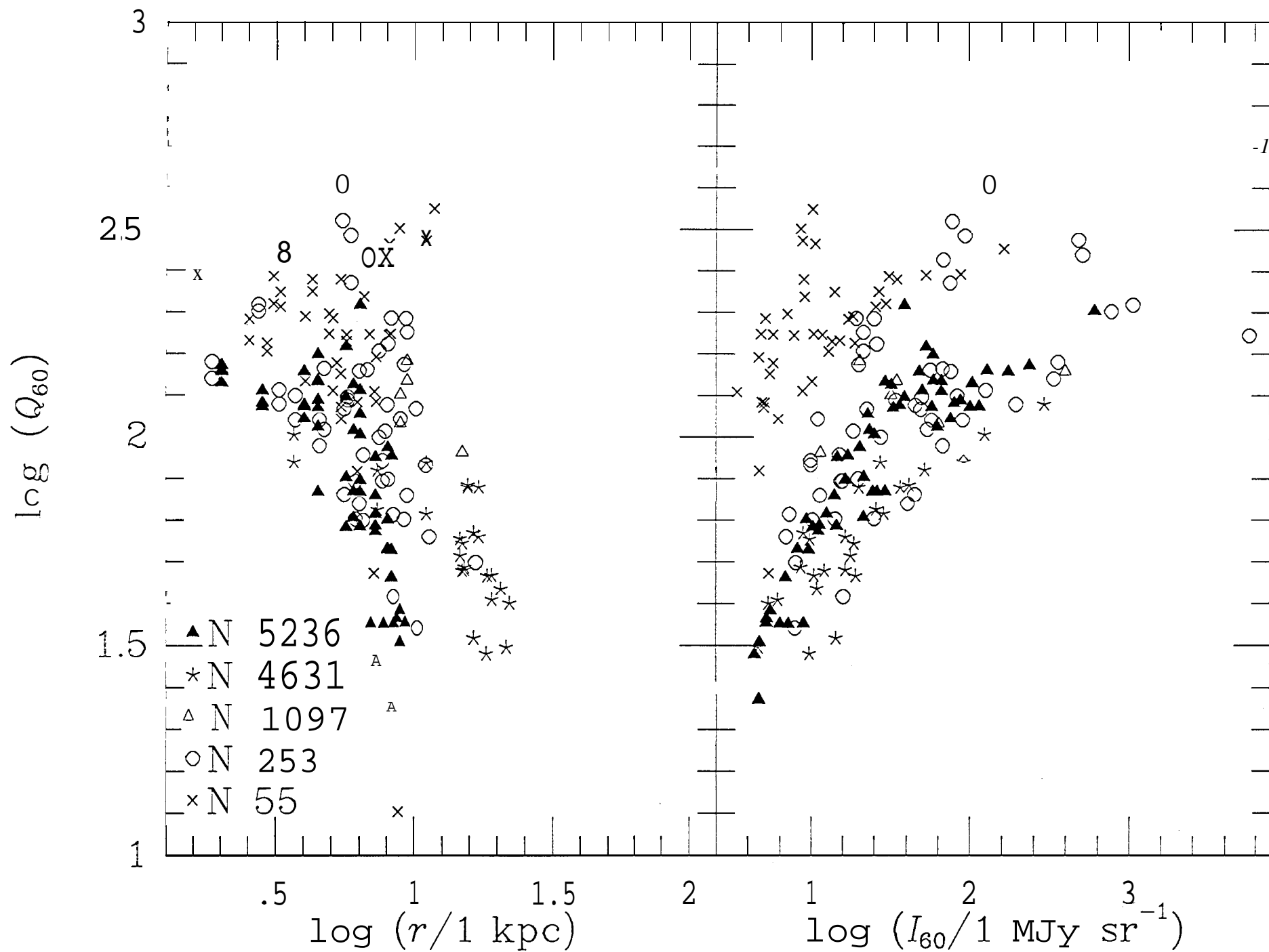


Fig 4e

Fig 5

